Applied Catalysis B: Environmental 129 (2013) 382–393

Contents lists available at SciVerse ScienceDirect

Applied Catalysis B: Environmental

journal homepage: www.elsevier.com/locate/apcatb

Stabilization mechanism and crystallographic sites of Ru in Fe-promoted barium hexaaluminate under high-temperature condition for N_2O decomposition

Yan Zhang[a,b], Xiaodong Wang[a,*], Yanyan Zhu[c], Tao Zhang[a,*]

[a] State Key Laboratory of Catalysis, Dalian Institute of Chemical Physics, Chinese Academy of Sciences, Dalian 116023, People's Republic of China
[b] Graduate University of Chinese Academy of Sciences, Beijing 100049, People's Republic of China
[c] College of Chemical Engineering, Northwest University, Xi'an 710069, People's Republic of China

ARTICLE INFO

Article history:
Received 18 June 2012
Received in revised form
14 September 2012
Accepted 1 October 2012
Available online 8 October 2012

Keywords:
Stabilization of ruthenium
Hexaaluminate
Iron
Rietveld refinement
N_2O decomposition

ABSTRACT

The stabilization of volatile ruthenium from catalysts at high temperatures is an important issue in both academia and industry. In this paper, Ru-substituted barium hexaalumimates ($BaRu_{0.2}FeAl_{10.8}O_{19}$) with β_l-Al_2O_3 structure were prepared using the carbonates route and investigated for high-concentration of N_2O decomposition. It was for the first time found that the evaporation of ruthenium species under high-temperature condition (1100–1200 °C) could be effectively suppressed by the addition of Fe in the hexaaluminate precursor. Fe promoted the formation of intermediate stable $BaRuO_3$ phase, which greatly alleviated the evaporation of Ru species during calcination, and thus allowed more Ru species enter into the final sintering-resistant hexaaluminate lattice after high-temperature treatment. Ru ions in the hexaaluminate structure only occupied the distorted tetrahedral interstitial Al(5) sites in the loosely packed mirror plane, which originated from Ru species in oxidic entities dispersed on the Ba-modified γ-Al_2O_3 and the intermediate $BaRuO_3$ in the precursors. Ru ions in the Al(5) sites were key factors responsible for the high activity of N_2O decomposition.

1. Introduction

N_2O is being considered as a promising green propellant used for small satellite propulsion systems, due to its low toxicity compared with traditional hydrazine propellant, as well as its capability for self-pressurizing and compatibility with the common construction materials [1–3]. The chemistry for N_2O as a propellant lies in the decomposition of N_2O into N_2 and O_2 accompanies with a large amount of heat release and volume expansion, which can be used as propulsion power. Quite different from the abatement of environmental pollutant N_2O where the concentration of N_2O is only in ppm level [4–13], the N_2O used as the propellant must have a high-concentration, even being a pure chemical, so as to generate the propulsion power as high as possible. However, the decomposition of pure N_2O is a highly exothermic reaction (the enthalpy is −82 kJ/mol) and leads to a temperature rise over 1000 °C [1,14]. Therefore, for the N_2O decomposition applicable in propulsion systems, besides activity, the high-temperature stability of catalytic materials has become a paramount factor to be considered.

So far, most of N_2O catalytic decomposition studies are focused on environmental field with low N_2O concentration [15]. Various catalytic formulations have been proposed, including pure and mixed oxides [4–7], transition metal-exchanged zeolites [8–10], and supported metal catalysts [11–13]. Among them, Ru supported catalysts have been found to be very efficient. Li and Armor [11] investigated the catalytic activity of metal supported M/ZSM-5 catalysts for nitrous oxide decomposition, and found that the activity followed the order: Ru, Rh > Pd > Cu > Fe > Pt > Ni > Mn. Zeng and Pang [12] developed a low-content (0.2 wt.%) Ru catalyst on alumina support, which showed excellent catalytic performance for N_2O decomposition (4.8×10^4 μmol (N_2O) g^{-1} h^{-1} at 400 °C). Kawi et al. [13] reported that Ru/MCM-41 catalyst prepared from $Ru(OH)_3$ was highly active for the catalytic decomposition of N_2O, achieving a complete decomposition of N_2O at 400 °C using a loading of 5.0 wt.% Ru.

Although the Ru-based catalysts above-cited exhibited excellent N_2O decomposition activity at lower temperatures (≤600 °C), like most of the noble metal catalysts, they did not maintain a high thermal stability to withstand high-temperature treatment due to the inherent volatility of ruthenium. McCarty et al. [16] compared the vaporization partial pressures of noble metal containing species (Ir, Pd, Pt, Rh, and Ru) with O_2 at 0.5 atm, and found that Ru is the most volatile, followed by Ir, Rh, Pt, and Pd above 1000 °C. It would appear that the volatilization loss of Ru limits the use of

* Corresponding authors. Tel.: +86 411 84379680/84379015; fax: +86 411 84691570.
E-mail addresses: xdwang@dicp.ac.cn (X. Wang), taozhang@dicp.ac.cn (T. Zhang).

0926-3373/$ – see front matter © 2012 Elsevier B.V. All rights reserved.
http://dx.doi.org/10.1016/j.apcatb.2012.10.001

Ru-based catalysts under high-temperature operating conditions and potentially represents the limiting trade-off between high activity and long, active lifetime. For this point, the stabilization of volatile Ru at high temperatures has become an urgent technical issue for N_2O decomposition applicable in the propulsion systems.

Various efforts have been devoted to the stabilization of Ru under high-temperature conditions. Haynes et al. [17] prepared Ru-substituted catalyst (LSRuZ) with lanthanum–strontium–zirconate pyrochlore as a support through calcination at 1000 °C, and found that Ru could be stabilized in the pyrochlore structure by incorporating into the stable lanthanum–strontium–zirconate structure. Huang et al. [18] explored the structures of the RuO_x species supported on the stable monoclinic ZrO_2 (m-ZrO_2) after treatment in a wide temperature range of 400–1050 °C. They found that the Ru surface density could reach 0.2–2.2 Ru/nm^2, irrespective of the treatment temperatures, which was induced by the strong interaction between the RuO_x species and underlying m-ZrO_2 surface. These experimental findings indicated that one of suitable solutions to overcome the volatilization issue of Ru is to develop a suitable support which is sintering-resistant.

Various heat-resistant materials have been tested as catalysts or catalyst supports in the high-temperature catalytic process, such as spinel [19], perovskites [20], and hexaaluminate [21,22] et al. McCarty and co-workers [16,20] have investigated the sintering of a number of high-temperature supporting oxide powders and revealed that hexaaluminate powders have sintering resistance superior to all other oxide supports investigated, such as $MgAl_2O_4$ spinel, $LaAlO_3$, $SrZrO_3$, and $LaTiO_3$ perovskites. Hexaaluminate materials exhibit stable phase composition up to 1600 °C and remarkable resistance to sintering and thermal shock. These unique excellent properties are associated with their peculiar layered structure, consisting of alternate stacking along the *c* axis of closely packed spinel blocks and loosely packed mirror planes in which large cations are located [23,24]. More importantly, in hexaaluminate structure, there are various Al coordination sites available for substitution, and the introduction of transition or noble metal ions into the hexaaluminate structure by replacing Al^{3+} ions can enhance the catalytic activity without decrease of sintering resistance [25].

So far, most of the reports [26–29] have been concentrated on transition metal-substituted hexaaluminates, in which the oxide state and the crystallographic sites of substituted metals in structure were found to be closely related with the catalytic activity. Groppi et al. [26,27] observed that the combustion activity of CH_4 was enhanced with the increase of Mn^{3+}/Mn^{2+} ratio. Our previous work [28] also revealed that the octahedral Mn^{3+} in Al(1) site was much more active than tetrahedral Mn^{2+} in Al(2) site for N_2O decomposition. Recently, our group [29] proposed the mechanism of stabilization of Fe ions in Ba hexaaluminates, and indicated that Fe^{3+} ions in the Al(5) sites of β-Al_2O_3 and the Al(3) sites of MP phase were more active for N_2O decomposition than Fe ions in other crystallographic sites.

However, there are only few reports devoted to the noble metal-substituted hexaaluminates. Recently, it is found that the incorporation of noble metals into hexaaluminate can stabilize the noble metals against volatilization and then improve the catalytic activity, due to the strong interaction with hexaaluminate matrix. This endows the noble metal substituted hexaaluminate a combined advantage: high stability and high activity. Our previous work [30,31] demonstrated that, compared with those Ir species outside the hexaaluminate framework, the incorporated Ir species in the hexaaluminate structure greatly enhanced the N_2O decomposition activity. Kikuchi et al. [32] synthesized a homogeneous active species (such as Ni, Ru, Pt, and Pd) based hexaaluminate catalysts, and revealed that Ru could be stabilized in the hexaaluminate structure and the framework Ru improved the partial oxidation of CH_4. However, a series of issues, such as, how Ru ions were stabilized in the hexaaluminate structure, and which crystallographic sites were preferentially occupied by framework Ru and the connection with catalytic activity, were not discussed in details. In fact, to the best our knowledge, such study has not been performed in the system of noble metal-substituted hexaaluminates, although these issues are very important for understanding the stabilization mechanism of noble metals in hexaalumiante structure and thus the effects on the catalytic properties. This is probably due to the low content of the substituted noble metal for the large difference of radius and charge with Al^{3+} ions and the complex solid state reactions for the formation of hexaaluminate under elevated temperatures, both of which are very difficult to be characterized.

Rietveld refinement is a sensitive and widely used technique for doped crystal compounds [33]. In this paper, Ru-substituted Ba–Fe–Al hexaaluminates were prepared using the carbonates route, and an attempt has been made to explore the evolution of Ru from amorphous precursor to Ru-substituted barium hexaaluminate. It was for the first time found that the addition of Fe ions in the hexaaluminate precursor could greatly stabilize the Ru species even after 1200 °C calcination. Furthermore, the stabilization mechanism of Ru ions in Fe-promoted barium hexaaluminate under elevated temperatures was proposed on the basis of X-ray diffraction, Rietveld refinement, and ^{57}Fe Mössbauer spectroscopy. Finally, catalytic activity in high-concentration N_2O decomposition was investigated. These data are discussed in connection to the chemical state analysis of framework Ru with the aim to rationalize the catalytic properties of the materials.

2. Experimental

2.1. Catalyst preparation

$BaRu_{0.2}FeAl_{10.8}O_{19}$-*t* sample (denoted as BR0.2F1A-*t*, *t* indicates calcination temperature) was prepared using the carbonates route as reported [29,34]. $Ba(NO_3)_2$, $RuCl_3{\cdot}3H_2O$, $Fe(NO_3)_3{\cdot}9H_2O$, and $Al(NO_3)_3{\cdot}9H_2O$ with the molar ratio 1:0.2:1:10.8 were dissolved individually in deionized water at 60 °C, and then added into a saturated aqueous solution of $(NH_4)_2CO_3$ under strong stirring to form the hexaaluminate precursor precipitate. During the precipitation a considerable carbon dioxide generation was observed while the pH remained constant at a value of 7.5–8.0. After continuous stirring for 6 h and aging for 3 h at 60 °C, the precipitate was filtered, washed with deionized water, and dried at 120 °C overnight. The sample was then calcined at 500 °C, 700 °C, 900 °C, 1000 °C, 1100 °C, and 1200 °C for 4 h, to obtain BR0.2F1A-500, BR0.2F1A-700, BR0.2F1A-900, BR0.2F1A-1000, BR0.2F1A-1100, and BR0.2F1A-1200, respectively. To study the effect of Fe on the stabilization of Ru in Ru-substituted hexaaluminates, $BaRu_{0.2}Fe_xAl_{11.8-x}O_{19}$-*t* samples with different Fe content (*x* = 0.5, 0.8, denoted as BR0.2F0.5A-*t* and BR0.2F0.8A-*t*, respectively) were also prepared by the above-described procedure just by varying the amount of $Fe(NO_3)_3{\cdot}9H_2O$ and $Al(NO_3)_3{\cdot}9H_2O$ added.

For comparison, the $BaRu_{0.2}Al_{11.8}O_{19}$-*t* (denoted as BR0.2A-*t*), Ru/Al_2O_3-*t* samples were also prepared by the above co-precipitation procedure without $Fe(NO_3)_3{\cdot}9H_2O$ or/and $Ba(NO_3)_2$ in the starting materials. In addition, supported $Ru/BaFeAl_{11}O_{19}$ (denoted as Ru/BF1A) catalyst was prepared by impregnating the calcined $BaFeAl_{11}O_{19}$-1200 (denoted as BF1A-1200, prepared by the above co-precipitation method without $RuCl_3{\cdot}3H_2O$ in the starting materials) sample with $RuCl_3{\cdot}3H_2O$ solution. After drying at 120 °C overnight, the sample was then calcined in air at 500 °C for 4 h. The calcination at lower temperature (500 °C) made Ru component exist on the surface of hexaaluminate, instead of incorporating into the framework of hexaaluminate.

2.2. Catalyst characterization

The X-ray diffraction (XRD) patterns were recorded with a PANalytical X'Pert-Pro powder X-ray diffractormeter, using Cu K_α radiation (diffraction from a flat specimen, Bragg-Brentano arrangement, U = 40 kV, I = 40 mA) with Ni filter. The diffractograms were scanned between 2θ = 10–80°. Before XRD test, the sample was grind roundly to a fine powder and then pressed lightly using a glass slide, in order to alleviate the preferential orientation as possible arising from the anisotropic planar crystallites of hexaaluminates. The intensity distribution of obtained XRD pattern is close to that of standard $Ba_{0.75}Al_{11}O_{17.25}$ hexaaluminate (ICSD No. 29441, JCPDS No. 1-75-707). PDF database was used for phase analysis. Phase composition and the crystallographic sites of Fe and Ru ions were adjusted by Rietveld full-profile analysis using FULLPROF and RIETICA programs. In the Rietveld refinement process, the contributions of both the $K\alpha_1$ (λ = 1.54056 Å) and $K\alpha_2$ (λ = 1.54439 Å) radiations were considered, and the intensity ratio of $K\alpha_2/K\alpha_1$ was fixed to 0.5. Diffraction line profiles were approximated by Pseudo-Voigt function. The refined instrumental and structural parameters were: zero shift, scale factor, background polynomial parameters, unit cell parameter, FWHM and shape parameters, and site occupancies. Ionic scattering factors were used throughout the refinements. Site occupancy factors (SOF) were constrained to the chemical composition. The atomic coordinates were given based on the references (ICSD No. 29441 for β-Al_2O_3 phase and ICSD No. 75426 for $BaAl_2O_4$ phase).

The actual Ru loadings of the catalysts were determined by Thermo IRIS Interepid II inductively coupled plasma (ICP) after having dissolved solid in a mixture of concentrated acids (HCl + HNO_3).

BET surface areas of the catalysts were measured by N_2 adsorption at −196 °C using a Micromeritics ASAP 2010 apparatus.

Scanning electron microscopy (SEM) experiments were performed with a JSM 6360-LV electron microscope operating at 20–25 kV. The samples were vapor-deposited with gold before analysis.

The Mössbauer spectra were recorded at room temperature with a spectrometer working in the mode of constant accelerations with the use of ^{57}Co γ-quantum source in Rh matrix. The absorbers were obtained by pressing the powdered samples (about 10 mg/cm^2 of natural iron). Samples after H_2 reduction were protected under Ar during Mössbauer measurements. All spectra were computer-fitted to a Lorentzian shape with a least-squares fitting procedure. The isomer shifts (IS) were given with respect to the centroid of α-Fe at room temperature.

Transient response experiment was performed in a fixed-bed flow reactor. Prior to the experiment, a catalyst sample was pretreated in He flow at 300 °C for 1 h and then ascended to 400 °C. 5000 ppm of N_2O in He was then allowed to pass through the catalyst for a certain time. The outlet gas composition was monitored online by a mass spectrometer (Omini-star, GSD-300), with m/z of 44, 28 and 32 representing N_2O, N_2 and O_2, respectively.

2.3. Activity test

The catalytic tests on N_2O decomposition were carried out in a plug flow fixed-bed quartz reactor ($\Phi 10 \times 450$ mm) at atmospheric pressure as described previously [29]. Approximately 100 mg of a catalyst sample which was pelletized into grains of 20–40 meshes in order to reduce intraparticle diffusional limitations was placed on a quartz filter in the middle part of the quartz reactor. The catalyst was diluted with 400 mg of quartz sand of the same size to limit temperature gradients in the reactor. The reactor has been inserted into an electric furnace driven by a PID temperature controller/programmer (808P, China). The temperature of the catalyst has been measured and controlled by means of a K-type thermocouple (o.d. = 0.5 mm) sliding in a quartz thermocouple well (o.d. = 2 mm) directly fixed in the middle of the catalyst bed.

Prior to the reaction, the catalyst sample was pre-reduced with pure H_2 at 400 °C for 2 h. After cooling to room temperature in Ar, the gas flow was switched to the reacting gas mixture containing 30 vol.% N_2O in Ar at a flow rate of 50 ml/min, corresponding to a gas hour space velocity (GHSV) of 30,000 h^{-1}. The outlet gas composition was analyzed online with an Agilent 6890N gas chromatograph equipped with Porapak Q and Molecular Sieve 13X columns and a thermal conductivity detector. N_2O conversion was calculated from the difference between the inlet and outlet concentrations. Before analysis, the reaction proceeded at each temperature for 30 min to reach a steady state. To verify the reusability features of the catalyst, experiment was performed to re-test the catalyst recovered after the catalytic activity measurement. Before testing, the recovered catalyst was pre-reduced with the same procedure mentioned above. These steps were repeated three times to establish reusability of the catalyst.

3. Results and discussion

3.1. Effect of phase composition on the stabilization of Ru species

Fig. 1 shows the XRD patterns of Ru/Al_2O_3-t, BR0.2A-t, and BR0.2F1A-t samples, which were obtained by calcination of precursors at different temperatures.

For Ru/Al_2O_3 (Fig. 1a), samples calcined at 500 and 700 °C consisted of remarkable RuO_2 [JCPDS 1-88-286] peaks accompanied by broad modulations of the baseline corresponding to microcrystalline γ-Al_2O_3 [JCPDS 1-1308]. Increasing the calcination temperature, γ-Al_2O_3 was gradually transformed into θ-Al_2O_3 [JCPDS 35-121] and α-Al_2O_3 [JCPDS 1-71-1123], together with the consumption of RuO_2. After 1200 °C calcination, Ru/Al_2O_3 only presented rather sharp diffraction peaks of α-Al_2O_3 due to extensive sintering of particles.

In Ba-containing BR0.2A-500 and BR0.2A-700 (Fig. 1b), the diffraction peaks of RuO_2 and γ-Al_2O_3 were still observed, expect for a trace of microcrystalline barium oxidic species ($BaO_{1.86}$, [JCPDS 1-89-8423]) in BR0.2A-700. After calcination at 900 and 1000 °C, the appearance of remarkable $BaAl_2O_4$ peaks was observed, indicating that part of Ba compounds and γ-Al_2O_3 was transformed into $BaAl_2O_4$. Compared with the cell parameter a ($a = b$ = 10.435–10.441 Å) of $BaAl_2O_4$ in the Ru-free BA-900 and BA-1000 ($BaAl_{12}O_{19}$) samples [29], the corresponding values ($a = b$ = 10.435–10.441 Å) in BR0.2A-t (t = 900–1000 °C) did not get larger, indicating that larger Ru ions ($r(Ru^{4+})$ = 0.62 Å) did not enter into the rigid $BaAl_2O_4$ structure, probably due to the large difference of radius and charge with Al^{3+} ions (0.53 Å). In addition, weak peaks corresponding to δ-Al_2O_3 [JCPDS 46-1215] were also verified. Meanwhile, the intensity of RuO_2 diffraction peaks continuously decreased and eventually disappeared at 1100 °C, which was higher than the decomposition temperature (about 1000 °C) of RuO_2 [16]. As compared to Ru/Al_2O_3 (Fig. 1a), no α-Al_2O_3 was detected, implying that the presence of dispersed barium prevented sintering and transition of γ-Al_2O_3 to α-Al_2O_3 [35]. When the calcination temperature was raised to 1200 °C, the formation of a β-Al_2O_3 hexaaluminate phase took place, together with the consumption of γ-Al_2O_3 and $BaAl_2O_4$.

For BR0.2F1A (Fig. 1c), 500 °C calcination resulted in the similar phase composition as detected in BR0.2A-500, and no Fe oxide was detected. Taking into account the molar ratio of Ba:Ru:Fe:Al = 1:0.2:1:10.8 and high BET surface area (218 m^2/g) of the sample, Ru and Fe species should be dispersed on the Ba-modified γ-Al_2O_3. After calcination at 700 °C, besides

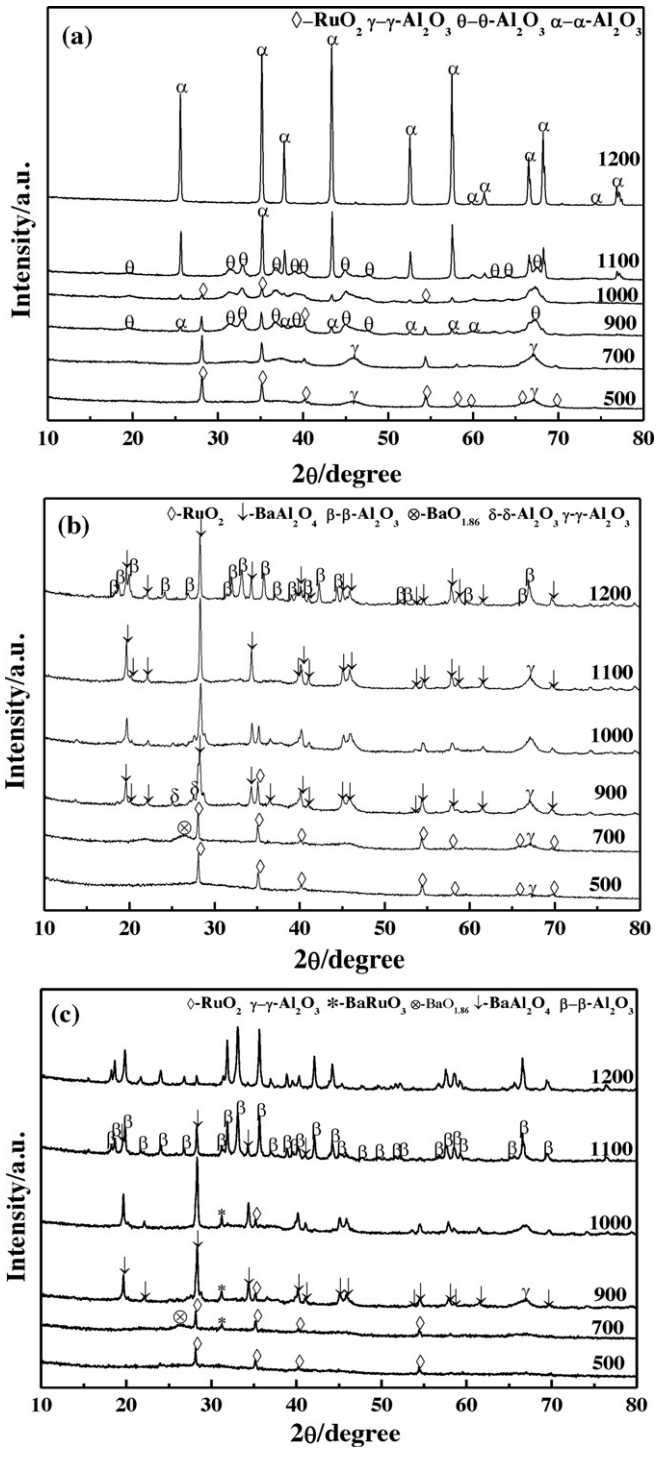

Fig. 1. X-ray diffraction patterns of: (a) Ru/Al_2O_3-*t*, (b) BR0.2A-*t*, and (c) BR0.2F1A-*t* samples.

$BaO_{1.86}$ compound as observed in BR0.2A-700, the diffraction peak ($2\theta = 31.2^\circ$) of $BaRuO_3$ appeared, indicating that part of Ba compounds and RuO_2 was transformed into $BaRuO_3$. This result strongly suggested that the introduction of Fe ions in the precursor resulted in the formation of the intermediate $BaRuO_3$ phase. It has been reported that, $BaRuO_3$ usually crystallized in three different hexagonal structures, that is, the nine-layer rhombohedral, four-layer hexagonal, and six-layer hexagonal polymorphs [36–38]. According to obtained XRD data, $BaRuO_3$ phase in our sample has a six-layer hexagonal perovskite structure with the same space group of $P6_3/mmc$ (No. 194) as that of β-Al_2O_3 hexaaluminate. This was in line with the previous literature [39], where the increase of Fe content, as well as the increase of pressure, favored the formation of $BaRuO_3$ phase with hexagonal perovskite structure ($P6_3/mmc$). Further calcination at 900 and 1000 °C, remarkable $BaAl_2O_4$ peaks were present. Like that in BR0.2A-900 and BR0.2A-1000, the larger Ru ions in BR0.2F1A-*t* (*t* = 900 and 1000 °C) were not incorporated into the rigid $BaAl_2O_4$ structure, since the cell parameters *a* (*a* = *b*) of $BaAl_2O_4$ in Ru-free BF1A-*t* [29] and BR0.2F1A-*t* (*t* = 900 and 1000 °C) were very close. In $BaAl_2O_4$ structure of BR0.2F1A-*t* (*t* = 900 and 1000 °C), only Fe ions ($r(Fe^{3+}) = 0.64$ Å) with similar radius and charge to Al^{3+} ions were located, which was confirmed by the expansion of cell parameters ($a = b = 10.441$–10.453 Å) of $BaAl_2O_4$ in BR0.2F1A-*t* compared with the Fe-free BR0.2A-*t* (*t* = 900 and 1000 °C) ($a = b = 10.435$–10.441 Å) samples. From the above results, one can see that there were two different Ru species in the precursors, that is, Ru species in oxidic entities dispersed on the Ba-modified γ-Al_2O_3, and Ru species located in the intermediate $BaRuO_3$ phase. Upon raising the calcination temperature to $t \geq 1100$ °C, the formation of a β-Al_2O_3 hexaaluminate phase took place together with the consumption of Ru species (RuO_2 and $BaRuO_3$), γ-Al_2O_3 and $BaAl_2O_4$. To be noted, such a formation temperature of hexaaluminate (1100 °C) was below the threshold temperature of 1200 °C observed in BR0.2A, which was attributed to the promoting effect of Fe on the mobility of Ba^{2+} in the γ-Al_2O_3 matrix [40]. Groppi et al. [35] proposed two routes for the formation of Ba-β-Al_2O_3 phases prepared by the co-precipitation method, namely solid-state reaction between γ-Al_2O_3 and dispersed barium compounds, or $BaAl_2O_4$. Considering the enlarged cell parameters of the hexaaluminate phase in BR0.2F1A-1100 and BR0.2F1A-1200 ($a = 5.613$–5.617 Å, $c = 22.772$–22.786 Å) than that in BR0.2A-1200 ($a = 5.592$ Å, $c = 22.747$ Å), Fe ions should be present in the hexaaluminate lattice, which originated from Fe species dispersed on the Ba-modified γ-Al_2O_3 and located in the intermediate $BaAl_2O_4$ phase, consistent with our previous report [29]. For Ru, it is noteworthy that no diffraction peaks corresponding to metallic Ru, RuO_2 or $BaRuO_3$ could be identified in BR0.2F1A-1100 and BR0.2F1A-1200 expect for the hexaaluminate phase, even the content of Ru was retained as high as 0.33–0.57 wt.% (determined by ICP), which probably caused by the incorporation of Ru species into the hexaaluminate structure. Therefore, similar mechanistic features can be reasonably invoked for the stabilization of Ru species in the final Ru-substituted Ba-hexaaluminate herein investigated, that is, Ru species in oxidic entities dispersed on the Ba-modified γ-Al_2O_3 and intermediate $BaRuO_3$ phase in the precursors may enter into the hexaaluminate structure through the solid-state reactions between Ba compounds and γ-Al_2O_3 during calcination.

For clarity, Fig. 2 displays the XRD patterns of BF1A-1200 and BR0.2F1A-1200 samples in the range from 27° to 37° (2θ). For comparison, Ru/BF1A was also characterized by XRD. Compared with Ru-free BF1A-1200 ($a = b = 5.614$ Å, $c = 22.775$ Å), the cell parameter of hexaaluminate in Ru/BF1A did not show any variability. Taking into account the presence of diffraction peaks around 28° and 35° corresponding to RuO_2 phase, 0.31 wt.% Ru loading (determined by ICP) probably existed as RuO_2 outside the framework of hexaaluminate. In contrast to Ru/BF1A, no any Ru species were detected in BR0.2F1A-1200 sample, although the latter has similar Ru loading (0.33 wt.%). From Fig. 2, one can see that the pattern of BR0.2F1A-1200 slightly shifted to lower 2θ values corresponding to the enlargement of the cell parameters ($a = b = 5.617$ Å, $c = 22.786$ Å) of β-Al_2O_3 hexaaluminate based on the Bragg equation ($2d \sin\theta = n\lambda$). This led to the conclusion that larger ruthenium cations ($r(Ru^{4+}) = 0.62$ Å) have been incorporated into the hexaaluminate lattice by replacing smaller Al^{3+} ions (0.53 Å). Since the oxidation state of ruthenium in the RuO_2 and $BaRuO_3$ precursors

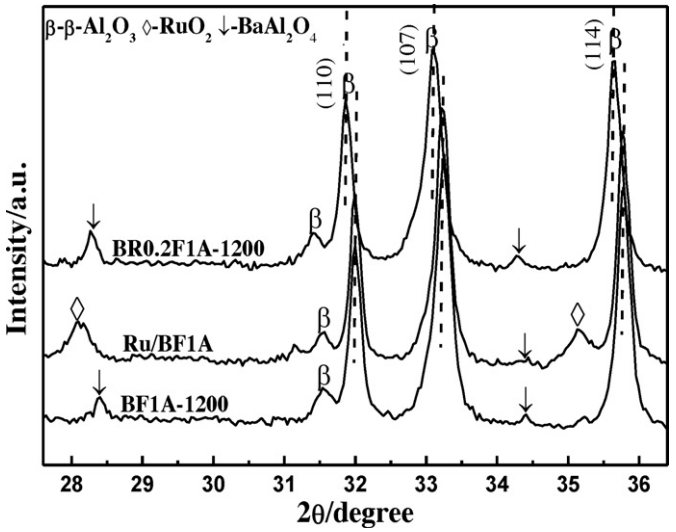

Fig. 2. X-ray diffraction patterns of BF1A-1200, BR0.2F1A-1200, and Ru/BF1A samples in the rang of 27–37° (2θ).

is Ru^{4+}, which is a stable oxidation state of ruthenium in oxide lattice [17], the introduced ruthenium in hexaaluminate structure probably existed as Ru^{4+}.

3.2. Morphology

The BET surface areas of Ru/Al_2O_3-*t*, BR0.2A-*t*, and BR0.2F1A-*t* samples are listed in Table 1. As expected, the BET surface areas of these samples decreased continuously with the elevation of the calcination temperature. In particular, significant sintering occurred accompanied with phase transformations, which resulted in a great loss in specific surface areas. For example, significant loss of surface area took place when the samples were calcined at 900 °C. As described above, phase transformation started at this temperature, i.e., γ-Al_2O_3 was transformed into θ-Al_2O_3 and α-Al_2O_3 for the Ru/Al_2O_3 sample, while $BaAl_2O_4$ phase formed for both the BR0.2A and BR0.2F1A samples. In addition, the introduction of Fe resulted in the loss of specific surface areas at the same calcination temperature, probably due to the promoting effect of Fe on the phase transformation. It must be stressed that both the BR0.2A-1200 and BR0.2F1A-1200 (19–31 m^2/g) presented much larger surface areas than the Ru/Al_2O_3-1200 (8 m^2/g) did, demonstrating the outstanding sintering-resistant property of hexaaluminates. This could be further visualized from the SEM images in Fig. 3. In contrast to the extensive sintering of Ru/Al_2O_3-1200, BR0.2A-1200 and BR0.2F1A-1200 showed small anisotropic planar crystallites. The observed planar facet should have orientations parallel to the mirror plane, due to the peculiar layered structure of hexaaluminate which suppressed crystal growth along the *c*-axis [35].

Table 1
BET surface area of Ru/Al_2O_3-*t*, BR0.2A-*t*, and BR0.2F1A-*t* samples.

Calcination temperature (°C)	S_{BET} (m^2/g)		
	Ru/Al_2O_3	BR0.2A	BR0.2F1A
500	295	230	218
700	223	200	204
900	121	154	98
1000	120	138	91
1100	30	135	27
1200	8	31	19

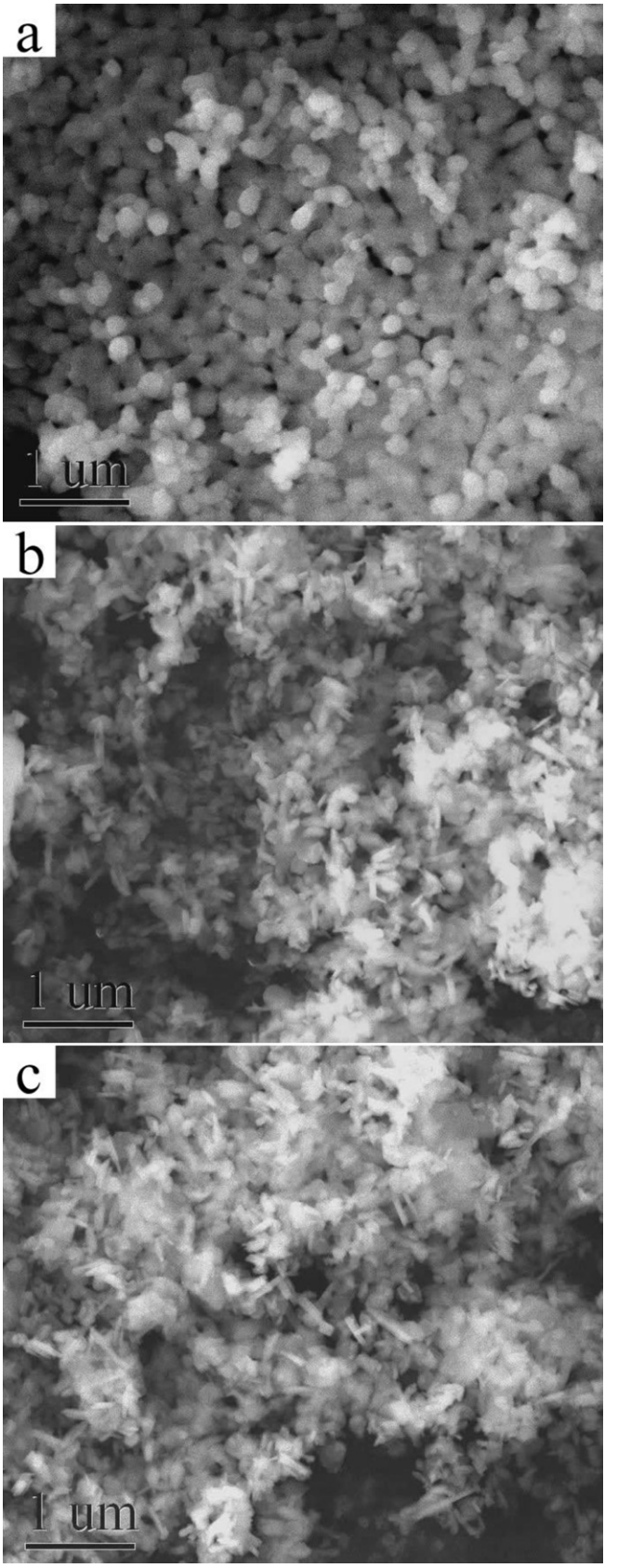

Fig. 3. Scanning electron micrographs of: (a) Ru/Al_2O_3-1200, (b) BR0.2A-1200 and (c) BR0.2F1A-1200 samples.

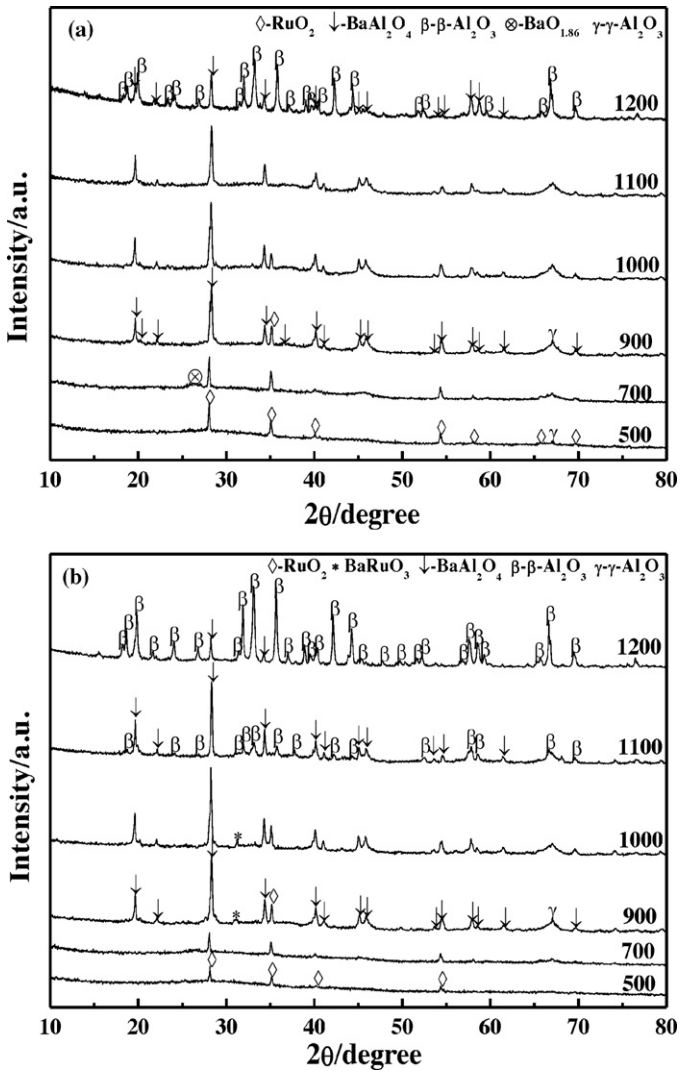

Fig. 4. X-ray diffraction patterns of (a) BR0.2F0.5A-*t* and (b) BR0.2F0.8A-*t* samples.

3.3. Effect of Fe ions on the stabilization of Ru species

As described above, the introduction of Fe into BR0.2A-*t* resulted in the formation of intermediate $BaRuO_3$ phase in BR0.2F1A-*t* during calcination. In order to investigate the effect of Fe on the formation of Ru-substituted Ba-hexaaluminate in more detail, the BR0.2F*x*A-*t* (*x* = 0.5 and 0.8, denoted as BR0.2F0.5A-*t* and BR0.2F0.8A-*t*, respectively) samples were also prepared and characterized by XRD. As shown in Fig. 4a, the $BaRuO_3$ phase was not detected in BR0.2F0.5A-*t*, which existed similar evolution of phase composition to that observed in BR0.2A-*t*. The tiny discrepancy between them lain in the addition of Fe decreased the relative intensity of impurity $BaAl_2O_4$ in the final hexaaluminate materials, indicating that Fe facilitated the formation of pure hexaaluminate. Increasing Fe content to *x* = 0.8 (BR0.2F0.8A-*t*, Fig. 4b), it is noteworthy that the intermediate $BaRuO_3$ phase was observed, although its intensity was very low. The diffraction peak of $BaRuO_3$ became sharper with further increasing the Fe content (*x* = 1, Fig. 1c). Obviously, both the appearance of intermediate $BaRuO_3$ phase at *x* = 0.8 and the increase of the intensity of corresponding diffraction peak at *x* = 1 were much related to the Fe content in the hexaaluminate precursor. These results unambiguously indicated that the increase of Fe content promoted the formation of intermediate $BaRuO_3$ phase during calcination. In addition, the increase of Fe content (*x* = 0.8 and 1) promoted the formation of the hexaaluminate phase that occurred at 1100 °C, below the threshold temperature of 1200 °C observed in BR0.2F*x*A (*x* = 0 and 0.5).

Percentage ruthenium content in BR0.2F*x*A-*t* (*x* = 0, 0.5, 0.8, and 1) was calculated by chemical analysis using inductive coupled plasma (ICP) spectrometer and the corresponding results are listed in Table 2. For comparison, Ru content of Ru/Al_2O_3-*t* samples was also summarized. One can see that Ru content continuously decreased with increasing calcination temperature, implying the evaporation of partial Ru component during calcination. For Ru/Al_2O_3, significant loss of Ru content occurred at 900 °C, corresponding to the weakening of RuO_2 peaks as shown in Fig. 1a. In particular, after calcination at 1100 and 1200 °C, Ru content were rather low, even below the detection limit of the analysis technique, indicating that Ru species could not stabilized by Al_2O_3 support under high-temperature condition. In the case of BR0.2A-*t*, significant loss of Ru content was also observed. However, after 1200 °C calcination with the formation of hexaaluminate phase, Ru content was a little higher than that in Ru/Al_2O_3, indicating that the evaporation of Ru component was suppressed to some extent due to the formation of hexaaluminate phase. Compared with BR0.2A-*t*, BR0.2F0.5A-*t* remained a little more Ru content at the same calcination temperature, although both of them existed similar phase composition as shown in Figs. 1b and 4a, indicating that the addition of Fe component in the precursor was beneficial to the stabilization of Ru species under high-temperature condition. Increasing Fe content to *x* = 0.8 (BR0.2F0.8A-*t*), the Ru content further increased from 0.26–0.31 wt.% at *x* = 0.5 to 0.33–0.38 wt.% after calcination at 900 and 1000 °C. When the Fe content increased up to *x* = 1 (BR0.2F1A-*t*), the remaining Ru content even reached as high as 0.65–0.67 wt.%, just slightly lower than the original values (0.68–0.78 wt.%, calcined at 500–700 °C). Taking into account the formation of intermediate $BaRuO_3$ phase at these temperatures in both samples, the maintenance of higher Ru content in BR0.2F0.8A-*t* and BR0.2F1A-*t* (*t* = 900 and 1000 °C) should be attributed to the stabilization effect of $BaRuO_3$ structure, which can resist high-temperature treatment [36,37]. This was further supported by the fact that, the increase of Ru content in BR0.2F0.8A-*t* and BR0.2F1A-*t* (*t* = 900 and 1000 °C) was proportional to the increased intensity of $BaRuO_3$ diffraction peak as revealed by XRD patterns (Figs. 1c and 4b). Obviously, the formation of intermediate $BaRuO_3$ phase promoted by the increase of Fe content greatly alleviated the evaporation of Ru species during calcination, and thus remained higher initial amount of Ru species which may enter into the final sintering-resistant hexaaluminate lattice after high-temperature treatment. When the calcination temperature was increased to 1100 and 1200 °C with the formation of hexaaluminate phase, BR0.2F0.8A and BR0.2F1A still retained 0.11–0.23 wt.% and 0.33–0.57 wt.% Ru content, respectively, which were 5.5–7.7 and 16.5–19 times larger than those in BR0.2A-1200 and BR0.2F0.5A-1200 with hexaaluminate structure (0.02–0.03 wt.%). To our knowledge, this is the first report that the introduction of Fe ions in the hexaaluminate precursor greatly promoted the stabilization of Ru species under high-temperature condition. As for such a promoting effect of Fe, two important factors should be considered. Firstly, the addition of Fe ions transformed the existing form of Ru species from easily volatile RuO_2 to stable intermediate $BaRuO_3$ phase, and thus more Ru species was stabilized in the hexaaluminate precursor. The formation of intermediate $BaRuO_3$ phase was regarded as the key factor for the stabilization of Ru species under high-temperature condition. Secondly, Fe promoted the formation of final hexaaluminate structure at lower calcination temperature (1100 °C), and the formed hexaaluminate structure suppressed the evaporation of Ru component to some extent via the

Table 2
Ru content of Ru/Al_2O_3-*t* and BR0.2FxA-*t* (*x* = 0, 0.5, 0.8, and 1) samples.

Calcination temperature (°C)	Ru content (wt.%)				
	Ru/Al_2O_3	BR0.2A	BR0.2F0.5A	BR0.2F0.8A	BR0.2F1A
500	0.97	0.81	0.86	0.79	0.78
700	0.86	0.73	0.75	0.72	0.68
900	0.20	0.29	0.31	0.38	0.67
1000	0.16	0.22	0.26	0.33	0.65
1100	0.01	0.05	0.07	0.23	0.57
1200	–	0.02	0.03	0.11	0.33

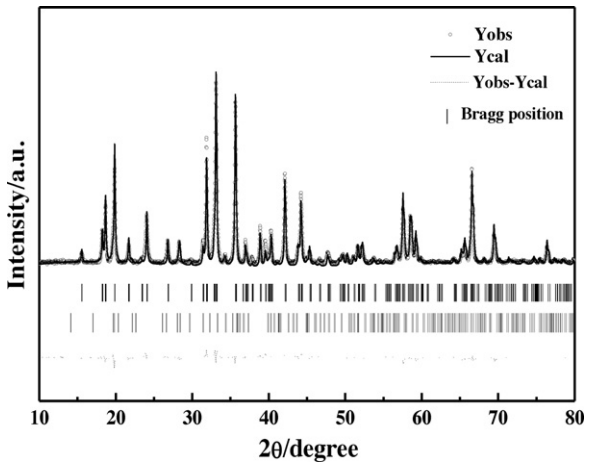

Fig. 5. X-ray diffraction patterns fitted using the Rietveld refinement method for BR0.2F1A-1200 sample. The upper tick marks corresponding to β-Al_2O_3, the lower tick marks corresponding to $BaAl_2O_4$.

strong interaction between framework Ru and the hexaaluminate lattice.

3.4. Identification of Ru crystallographic sites in barium hexaaluminate

3.4.1. Rietveld refinement

The incorporation of Ru ions into the hexaaluminate structure plays an important role in the stabilization of Ru species under high-temperature condition. Sequentially, Rietveld refinement was employed to identify the crystallographic sites of framework Ru, since Rietveld refinement is a powerful tool to identify the crystalline structure and crystalline phase abundance [33]. Fig. 5 displays the XRD pattern fitted using the Rietveld refinement method for BR0.2F1A-1200 sample, and the corresponding results are summarized in Tables 3 and 4. One can see that the BR0.2F1A-1200 sample consisted of 97.78% β-Al_2O_3 hexaaluminate and 2.22% $BaAl_2O_4$ phase.

For unsubstituted Ba-β-Al_2O_3, the existence of two different phases, β_I and β_{II}, with different Ba contents have been demonstrated [41]. In Ba-poor samples the β_I phase with composition $Ba_{0.75}Al_{11}O_{17.25}$ forms while in Ba-rich samples the β_{II} phase with composition $Ba_{1.167}Al_{10.667}O_{17.167}$ forms. Based on the XRD data we obtained, the Ba-poor Ba-β_I-Al_2O_3 structure was chosen as starting model for the Rietveld refinement of BR0.2F1A-1200. The analysis results confirmed that a Ba-poor β_I-Al_2O_3 phase with $Ba_{0.76}Ru_{0.02}Fe_{0.79}Al_{10.19}O_{17.24}$ (Table 3) indeed formed in BR0.2F1A-1200, in line with the previous literature [42]. In Ba-poor β_I-Al_2O_3 structure (Fig. 6), small fractions of Al^{3+} ions shifted from their normal octahedral Al(1) sites in the spinel block to new tetrahedral interstitial Al(5) sites in the mirror plane bridged by interstitial oxygen due to the vacancy of Ba^{2+} through a Reidinger defect mechanism [41]. Similar with the distribution of Fe in BF1A-1200 [29], the refinement of our data also revealed that Fe ions in BR0.2F1A-1200 sample occupied both the symmetric tetrahedral Al(2) sites in the spinel block and the distorted tetrahedral interstitial Al(5) sites in the mirror plane (Table 4). Different from the occupation of Fe, Ru only occupied the tetrahedral interstitial Al(5) sites in the mirror plane arising from Reidinger defect, while Al(1), Al(2), Al(3), and Al(4) sites did not show any significant evidence of

Table 3
Structural refinement results of BR0.2F1A-1200 sample.

R_p	13.966
R_{wp}	16.154
Phase composition (molar ratio)	97.78% β_I-Al_2O_3[a], 2.22% $BaAl_2O_4$
Composition of β_I-Al_2O_3 phase	$Ba_{0.76}Ru_{0.02}Fe_{0.79}Al_{10.19}O_{17.24}$
a = *b* (Å)	5.617
c (Å)	22.786

[a] One type of β-Al_2O_3 hexaaluminate.

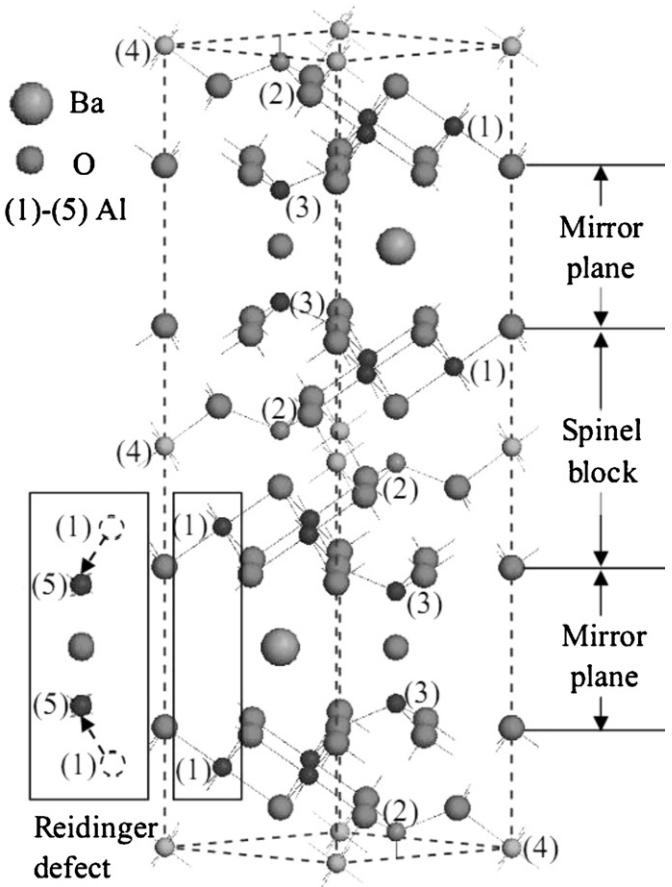

Fig. 6. The structure of β_I-Al_2O_3 hexaaluminate. Numbers in parenthesis refer to the different Al sites. Al(1), octahedral site; Al(2), tetrahedral site; Al(3), tetrahedral site; Al(4), octahedral site; Al(5), tetrahedral site.

Table 4
Refined sites occupancy of Ba, Fe, Ru, and Al in Ba-β-Al_2O_3 of BR0.2F1A-1200 sample.

Atom site	Mult.[a]	Site	Coor.[b]	Atomic coordinates			Site occupancy
				X	*Y*	*Z*	
Ba(1)	2	2d	–	0.3333	0.6667	0.75	0.763
Al(1)	12	12k	Oh[c]	0.1676	0.3351	−0.1046	0.921
Al(2)	4	4f	Th[d]	0.3333	0.6667	0.0235	0.799
Al(3)	4	4f	Oh	0.3333	0.6667	0.1756	1.00
Al(4)	2	2a	Oh	0	0	0	1.00
Al(5)	12	12k	Th	0.8453	0.6906	0.1780	0.010
Fe in Al(2)	4	4f	Th	0.3333	0.6667	0.0235	0.201
Fe in Al(5)	12	12k	Th	0.8453	0.6906	0.1780	0.065
Ru in Al(5)	12	12k	Th	0.8453	0.6906	0.1780	0.004
O(1)	4	4e	–	0	0	0.1413	1.00
O(2)	4	4f	–	0.3333	0.6667	−0.0554	1.00
O(3)	2	2c	–	0.3333	0.6667	0.2500	1.00
O(4)	12	12k	–	0.1582	0.3164	0.0495	1.00
O(5)	12	12k	–	0.5036	0.0073	0.1474	1.00
O(6)	6	6h	–	0.8855	0.7710	0.2500	0.079

[a] Multiplicity.
[b] Coordination.
[c] Octahedral.
[d] Tetrahedral. Constrains on occupancies of β_I-Al_2O_3 phase relevant to Reidinger defect mechanism (Ba(1) + 3Al(5)[e] = 1, Al(5)[e] = O(6), Al(1) + Al(5)[e] = 1, [e]Fe and Ru occupancy in Al(5) must be included) in Ref. [42].

Ru substitution (Table 4). Such a difference should originate from different chemical states of Ru and Fe in the precursors.

Our previous work [29] had given a clear picture of the evolution of Fe ions. In order to compare the distinctness between the distribution of Ru and Fe ions, the schematic diagram of the evolution of Ru and Fe ions from precursors to different crystallographic sites of substituted barium hexaaluminate was proposed. As shown in Fig. 7, initially, both Ru and Fe species were dispersed on the Ba-modified γ-Al_2O_3 existing as oxidic entities. With the formation of intermediate $BaRuO_3$ and $BaAl_2O_4$ phases as increasing the calcination temperature, Ru ions partially migrated into the hexagonal perovskite-type structure of $BaRuO_3$, while part of Fe ions incorporated into the spinel-type $BaAl_2O_4$ structure. When β_I-Al_2O_3 type hexaaluminates formed at higher calcination temperature, Ru and Fe ions existed as the oxidic entities dispersed on the Ba-modified γ-Al_2O_3 mainly entered into the Al(5) sites in the Ba-containing mirror plane of hexaaluminates via the diffusion of Ba^{2+} ions in γ-Al_2O_3, since the mirror plane is loosely packed in a way favorable to ion diffusion [29]. Meanwhile, Ru ions in the $BaRuO_3$ structure also preferentially entered into the distorted Al(5) sites in the mirror plane through solid-state reaction between Ba compounds ($BaRuO_3$) and γ-Al_2O_3, based on the similar structure of $BaRuO_3$ and hexaaluminate with same space group ($P6_3/mmc$). However, Fe ions in $BaAl_2O_4$ spinel incorporated into the tetrahedral Al(2) sites in the spinel block of hexaaluminates, rather than migrating into other Al sites, due to the strong structural similarity between spinel and spinel block of hexaaluminate, consistent with our previous report [29].

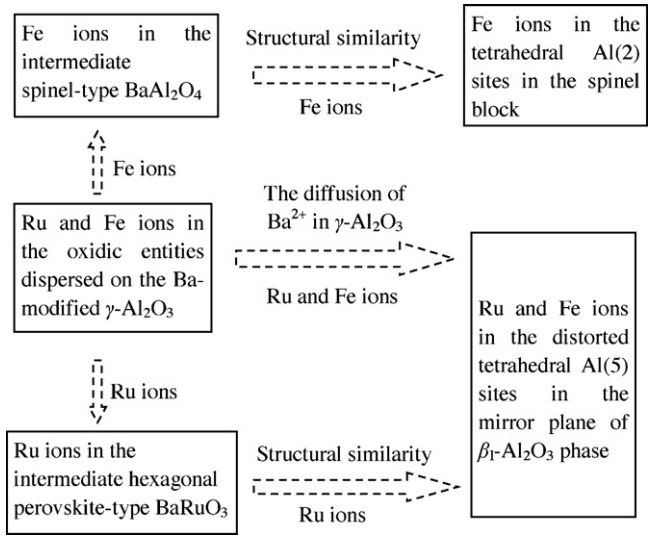

Fig. 7. The schematic diagram of the evolution of Ru and Fe ions from precursors to different crystallographic sites of substituted barium hexaaluminate.

According to Pauling's electrostatic valence rule [41], the ideal valence of the large cation in the mirror plane required for the stoichiometric Ba-poor β_I-Al_2O_3 structure can be estimated and found to be +1.5, which is lower than the actual charge (+2.0) of large Ba^{2+} cation. To maintain electroneutrality with respect to the more positive charge provided by Ba^{2+}, a quarter of the Ba^{2+} in the mirror plane (Beevers-Ross sites) is replaced by O^{2-} (Reidinger defects), leading to the shift of small fractions of Al^{3+} ions from Al(1) sites to interstitial Al(5) sites (Fig. 6). Compared to the site occupancy of Ba in BF1A-1200 (78.7%) [29], the value in BR0.2F1A-1200 was lower (76.3%, Table 4), suggesting that the substitution of Ru ions resulted in more Ba^{2+} vacancy. Therefore, more new tetrahedral interstitial Al(5) sites in the mirror plane formed through Reidinger defect mechanism. In a word, the replacement of Al^{3+} by Ru^{4+} brought about more tetrahedral interstitial Al(5) sites in the mirror plane through charge compensation mechanism, which was occupied by Ru^{4+} ions, and thus Ru^{4+} ions were stabilized in hexaaluminate structure.

3.4.2. ^{57}Fe Mössbauer spectroscopy

In the hexaaluminate structure, both framework Ru and Fe ions are coordinated with lattice oxygen, and thus their chemical state may be influenced by each other. Since Fe can be studied by sensitive ^{57}Fe Mössbauer spectroscopy, the local chemical environment of ruthenium in the framework may be investigated indirectly through the analysis of Fe chemical state. Fig. 8 displays the room temperature fitted ^{57}Fe Mössbauer spectra of BF1A-1200, BR0.2F1A-1200, and Ru/BF1A samples after H_2 reduction at 350 °C for 2 h. For comparison, these synthesized fresh samples were also characterized by ^{57}Fe Mössbauer spectroscopy. The corresponding Mössbauer parameters are listed in Table 5.

For BF1A-1200, the spectrum was fitted with two doublets, which were assigned to different tetrahedral (Th) Fe^{3+} species in the β_I-Al_2O_3 structure, because both of IS values (IS = 0.21–0.23 mm/s) were very close to Fe^{3+} in tetrahedral sites (IS = 0.19–0.23 mm/s)

Table 5
Room temperature ^{57}Fe Mössbauer parameters of BF1A-1200, BR0.2F1A-1200 and Ru/BF1A samples after H_2 reduction at 350 °C for 2 h.

Samples	IS[a] (mm/s)	QS[b] (mm/s)	A[c] (%)	Assignment	Ratio[e]
BF1A-1200	0.23	1.01	49	Fe^{3+}(Th) in Al(5) of β_l-Al_2O_3	–
	0.21	0.60	51	Fe^{3+}(Th) in Al(2) of β_l-Al_2O_3	
BF1A-1200-red 350 °C[d]	0.25	0.98	28	Fe^{3+}(Th) in Al(5) of β_l-Al_2O_3	2.1
	0.23	0.62	41	Fe^{3+}(Th) in Al(2) of β_l-Al_2O_3	
	0.91	1.11	31	Fe^{2+}	
BR0.2F1A-1200	0.23	1.02	50	Fe^{3+}(Th) in Al(5) of β_l-Al_2O_3	–
	0.21	0.60	50	Fe^{3+}(Th) in Al(2) of β_l-Al_2O_3	
BR0.2F1A-1200-red 350 °C	0.23	1.12	14	Fe^{3+}(Th) in Al(5) of β_l-Al_2O_3	12
	0.24	0.73	47	Fe^{3+}(Th) in Al(2) of β_l-Al_2O_3	
	0.90	1.09	39	Fe^{2+}	
Ru/BF1A	0.23	1.01	49	Fe^{3+}(Th) in Al(5) of β_l-Al_2O_3	–
	0.21	0.60	51	Fe^{3+}(Th) in Al(2) of β_l-Al_2O_3	
Ru/BF1A-red 350 °C	0.23	1.04	30	Fe^{3+}(Th) in Al(5) of β_l-Al_2O_3	1.6
	0.22	0.66	39	Fe^{3+}(Th) in Al(2) of β_l-Al_2O_3	
	0.88	1.15	31	Fe^{2+}	

[a] Isomer shift relative to α-Fe.
[b] Quadrupole splitting.
[c] Relative area.
[d] The BF1A-1200 sample after H_2 reduction at 350 °C.
[e] The ratio of Fe^{2+} species in the Al(5) sites to those in the Al(2) sites, uncertainty is ±3% of reported value.

as reported in $LaFeAl_{11}O_{19}$ [43]. Since the higher QS value means the greater extent of anisotropic distortion around Fe^{3+} [43,44], one doublet with a small QS value (0.60 mm/s) was assigned to Fe^{3+}(Th) in the symmetric Al(2) sites in the spinel block, while the other doublet with relatively high QS value (1.01 mm/s) was assigned to Fe^{3+} ions in the distorted tetrahedral interstitial Al(5) sites in the mirror plane resulting from Reidinger defect. After reduction with H_2 at 350 °C for 2 h, one new iron component with IS = 0.91 mm/s and QS = 1.11 mm/s appeared, which was assigned to Fe^{2+} species [43]. Compared to the BF1A-1200 sample (51% and 49%), the relative area (A) of Fe^{3+} ions in the Al(2) and Al(5) sites of β_l-Al_2O_3 over the reduced BF1A-1200 sample decreased to 41% and 28%, respectively. Namely, 21% Fe^{3+} ions in the Al(5) sites in the mirror plane were reduced to Fe^{2+}, while only 10% Fe^{3+} ions in the Al(2) sites in the rigid spinel block was reduced. Obviously, Fe^{3+} ions in Al(5) sites in the mirror plane were much more easily reduced than those in Al(2) sites in the spinel block, since the mirror plane was a preferential diffusion route of oxygen [43].

In the case of BR0.2F1A-1200 and Ru/BF1A samples, like BF1A-1200, the observed two quadrupole doublets were assigned to tetrahedral Fe^{3+} species in the Al(2) and Al(5) sites in the β_l-Al_2O_3 structure, respectively, in line with our previous Rietveld refinement results. After H_2 reduction at 350 °C for 2 h, the preferential reduction of Fe^{3+} ions in Al(5) sites in the mirror plane was also observed. To be noted, the ratio of reducible Fe^{3+} amount in the Al(5) sites to those in the Al(2) sites in BR0.2F1A-1200 was as high as 12 (Table 5), which was much higher than those in BF1A-1200 sample (2.1), indicating that the presence of framework Ru significantly promoted the preferentially reduction of Fe^{3+} ions in the Al(5) sites. It was reasonable considering that only Fe^{3+} ions occupied the Al(2) sites in the spinel block, and in the mirror plane both Ru and Fe ions were located in the Al(5) sites and coordinated with lattice oxygen. Under reduction atmosphere, the adsorptive activation of H_2 onto the framework Ru ions in the Al(5) sites in the mirror plane probably promoted the removability of nearby lattice oxygen in the loosely packed mirror plane (the preferential diffusion route of oxygen). This resulted in the preferential reduction of adjacent Fe^{3+} ions in Al(5) sites in the same mirror plane, instead of the remote Fe^{3+} ions in Al(2) sites in the rigid spinel block. The above results further confirmed that Ru ions in BR0.2F1A-1200 were located in the Al(5) sites in the mirror plane, in line with the Rietveld refinement (Table 4). Unlike BR0.2F1A-1200, Ru/BF1A did not show significant selective reduction of Fe^{3+} ions in the Al(5) sites (Table 5), almost similar to that in BF1A-1200, probably because Ru was randomly dispersed outside of hexaaluminate.

3.5. Effect of chemical state of Ru on catalytic performance of N_2O decomposition

Fig. 9 depicts the profiles of 30 vol.% N_2O conversion versus the reaction temperature over Ru/Al_2O_3-1200, BF1A-1200, Ru/BF1A, and BR0.2F1A-1200 catalysts. The Ru/Al_2O_3-1200 catalyst was almost catalytically inactive towards N_2O decomposition until 650 °C. This could be attributed to the extreme vaporization of Ru species after high-temperature (1200 °C) treatment (Table 2) and the significant sintering of alumina support which was irreversibly converted to α-Al_2O_3 (Fig. 1a). The higher N_2O conversions were observed for BF1A-1200, Ru/BF1A, and BR0.2F1A-1200, demonstrating the superior textual properties of hexaaluminate than alumina support. In this case, an attempt has been made to correlate the location of Ru with the catalytic performances of BF1A-1200, BR0.2F1A-1200 and Ru/BF1A catalysts (Table 6). In the absence of Ru ($x = 0$), the BF1A-1200 did not exhibit activity towards N_2O decomposition until 550 °C. When 0.31 wt.% Ru loading was supported onto the BF1A-1200, a slight enhancement in the catalytic activity was observed. For example, the N_2O conversion at 550 °C was only increased from 6% (for Ru-free BF1A-1200) to 22%, implying that the supported Ru was less active for N_2O decomposition. To be noted, when similar Ru loading (0.33 wt.%) was incorporated into BR0.2F1A-1200 hexaaluminate structure, the activity was enhanced significantly and N_2O conversion even could attain 100% at 550 °C, suggesting that framework Ru species greatly promoted the N_2O decomposition activity. This was further confirmed by the calculated reaction rate at 400 °C on the basis of the amount of Ru

Table 6
Relationship between the location of Ru and catalytic performances of BF1A-1200, Ru/BF1A and BR0.2F1A-1200 catalysts.

Samples	Actual Ru[a] (mol/g_{Cat})	N_2O conversion at 550 °C (%)	R^b ($mol\,h^{-1}\,g_{Ru}{}^{-1}$)
BF1A	–	6	–
Ru/BF1A	3.07×10^{-5}	22	8.76
BR0.2F1A	3.26×10^{-5}	100	25.04

[a] The value determined by ICP.
[b] Reaction rate, which was calculated on the basis of the amount of Ru; reaction temperature: 400 °C.

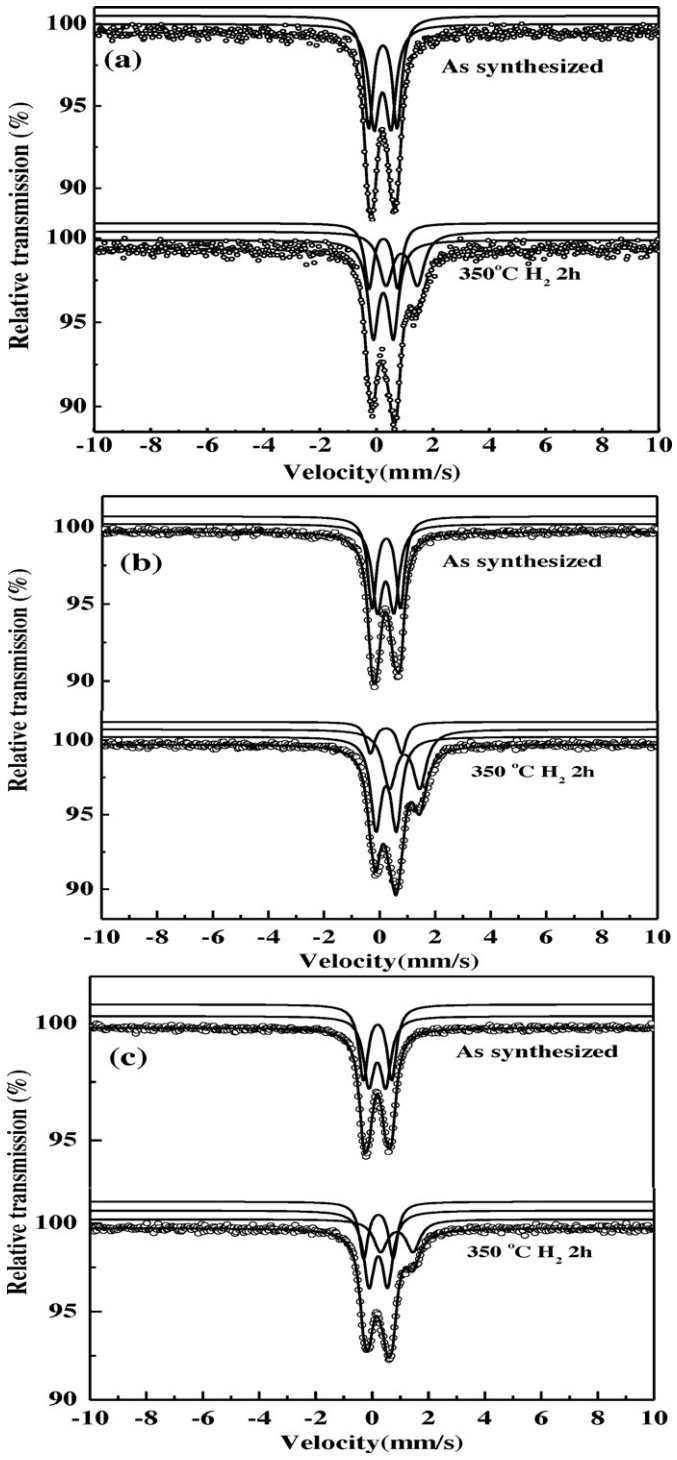

Fig. 8. Room temperature ^{57}Fe Mössbauer spectra of (a) BF1A-1200, (b) BR0.2F1A-1200 and (c) Ru/BF1A after H_2 reduction at 350 °C for 2 h.

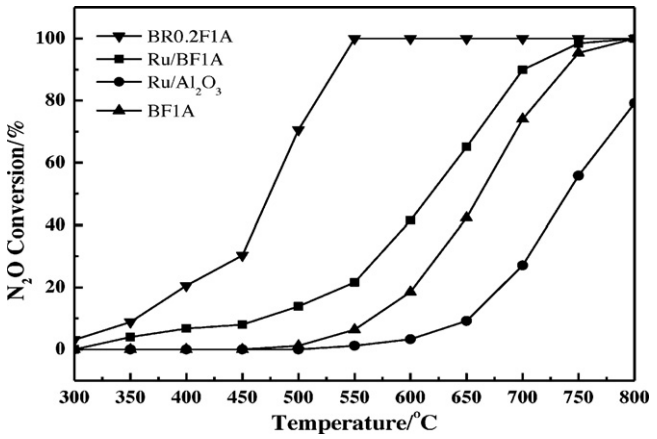

Fig. 9. N_2O conversion as a function of reaction temperature over Ru/Al_2O_3-1200, BF1A-1200, Ru/BF1A, and BR0.2F1A-1200 catalysts.

in different locations (Table 6). When Ru species were supported onto hexaaluminate (Ru/BF1A) existing as RuO_2 outside of hexaaluminate framework, the reaction rate was only 8.76 mol h^{-1} $g_{Ru}{}^{-1}$. This was reasonable considering that surface Ru species was easily agglomerated together during calcination, which was supported by the CO-chemisorption experiment where surface Ru on the Ru/BF1A was too large to be able to adsorb CO molecule. Therefore, the low activity of surface Ru species can be attributed to its large particle size (46 nm) determined by Scherrer formula. However, when Ru was incorporated into the hexaaluminate lattice, the reaction rate reached as high as 25.04 mol h^{-1} $g_{Ru}{}^{-1}$, suggesting that framework Ru ions in the Al(5) sites in the mirror plane of hexaaluminate were highly active for N_2O decomposition.

To uncover the underlying reason of such an enhancement effect of framework Ru species in the Al(5) sites on the N_2O decomposition activity, we performed the transient kinetic experiment. In order to maintain the N_2O conversions on the BR0.2F1A-1200 and Ru/BF1A catalysts at almost the same low values (<10%), transient responses of N_2O, N_2, and O_2 induced by a step variation in the concentration of N_2O were conducted at 400 °C, with W/F of 0.05 and 0.2 g s ml^{-1}, respectively. As shown in Fig. 10a, upon the flow gas being switched from He to N_2O/He, the evolution of N_2 ($m/z = 28$) and N_2O ($m/z = 44$) occurred instantly, indicating that N_2O decomposition to N_2 is a fast step. On the contrary, there was a significant delay in the appearance of O_2 ($m/z = 32$), implying that O_2 desorption from the catalyst surface is a rate-limiting step. It is interesting to note that such a delay in O_2 desorption became alleviated when Ru was incorporated into the hexaaluminate lattice, suggesting that the framework Ru in the Al(5) sites in the loosely packed mirror plane (the preferential diffusion route of oxygen) facilitates the desorption of oxygen (rate-limiting step) and thereby greatly enhances the catalytic activity.

According to the literature [14,45–47], the decomposition of N_2O can be described as the adsorption of N_2O at the active centers, usually coordinatively unsaturated surface noble metal ions, with the formation of N_2 and a surface O. Subsequently, this surface oxygen desorbs either by combination with another surface oxygen or by direct reaction with another N_2O. Based on this mechanism, there are two main factors affecting the N_2O decomposition activity of Ru-substituted hexaaluminate: the adsorption of N_2O onto surface Ru ions and the desorption of oxygen. Considering that the loosely packed mirror plane is a preferential exposure surface [48], Ru ions incorporated in the Al(5) sites in the mirror plane were easily accessible to the N_2O molecules and favorable for the adsorption of N_2O. On the other hand, the transient kinetic experiment results showed that the framework Ru in the Al(5) sites greatly facilitated the desorption of surface oxygen generated by the dissociative adsorption of N_2O, which is in agreement with our H_2-reduced ^{57}Fe Mössbauer results that the lattice oxygen close to Ru ions in the Al(5) sites in the mirror plane was much easier to move and diffuse. Therefore, Ru ions in Al(5) sites of β_1-Al_2O_3 phase, which were inlaid in the preferentially exposed mirror plane and coordinated with active oxygen that was easily to move and diffuse, should be highly active for N_2O decomposition.

For the application of Ru-substituted hexaaluminate in spacecraft propulsion systems, re-usability is another key parameter to

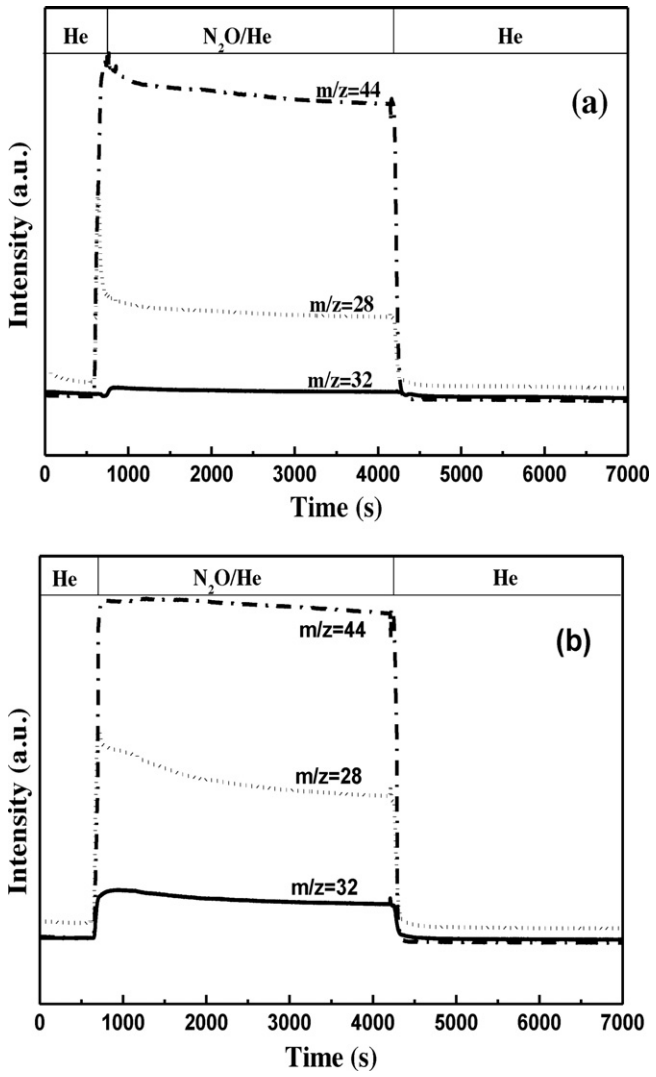

Fig. 10. Transient response curves of N_2O, N_2, O_2 induced by a step variation in the feeding composition over (a) Ru/BF1A, at 400 °C, $W/F = 0.2\ g\ s\ ml^{-1}$; (b) BR0.2F1A-1200, at 400 °C, $W/F = 0.05\ g\ s\ ml^{-1}$.

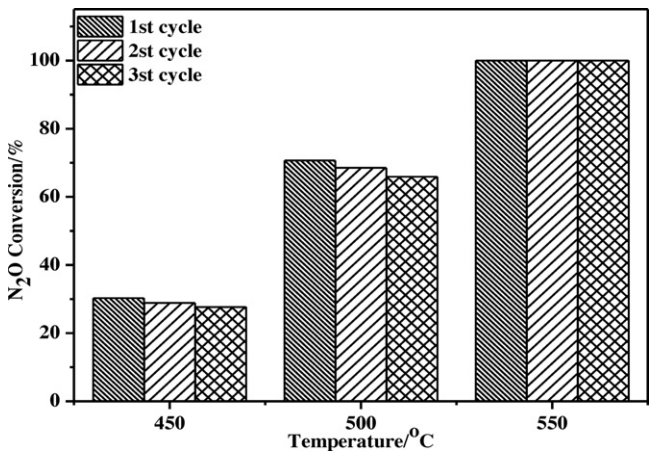

Fig. 11. N_2O conversions over BR0.2F1A-1200 at varying reaction temperatures in three cycles of reaction.

be considered. The regenerated catalyst was used for the decomposition of N_2O under similar reaction conditions as used for the as-calcined catalyst. No significant loss in the conversion of N_2O was observed up to three cycles at 450 °C, 500 °C, and 550 °C, respectively (Fig. 11), demonstrating a good re-usability of the BR0.2F1A-1200 catalyst. In a word, the excellent catalytic activity and high-temperature stability for N_2O decomposition make the Ru-substituted Ba-Fe-Al hexaaluminate a promising candidate for N_2O propellant decomposition.

4. Conclusion

In summary, we found that, for the first time, the introduction of Fe ions in the barium hexaaluminate precursor ($BaRu_{0.2}Fe_xAl_{10.8-x}O_{19}$, $x = 0$, 0.5, 0.8, and 1) could effectively suppress the evaporation of ruthenium species under high-temperature condition (1100–1200 °C). Increasing Fe content up to $x = 0.8$ and 1 transformed the existing form of Ru species in the precursor from easily volatile RuO_2 to stable intermediate $BaRuO_3$ phase, which was regarded as the key factor for the stabilization of Ru species under high-temperature condition. The formation of intermediate $BaRuO_3$ phase greatly alleviated the evaporation of Ru species during calcination, and thus allowed more Ru species enter into the final sintering-resistant hexaaluminate lattice and then more Ru species were stabilized after high-temperature treatment. Ru ions in hexaaluminate structure only occupied the distorted tetrahedral Al(5) sites, which originated from the intermediate hexagonal perovskite-type $BaRuO_3$ and Ru oxidic entities dispersed on the Ba-modified γ-Al_2O_3 in the precursors. The incorporation of Ru ions into β_I-Al_2O_3 hexaaluminate structure resulted in more tetrahedral Al(5) sites through the charge compensation mechanism, which are available for the occupation of Ru ions and thus Ru species were stabilized in the hexaaluminate structure. Ru ions in the Al(5) sites of β_I-Al_2O_3 hexaaluminates were key factors responsible for the high activity and stability of this Ru-substituted hexaaluminate catalyst in high-concentration (30 vol.%) N_2O decomposition reaction.

Acknowledgments

Financial support from National Science Foundation of China (NSFC) grants (21076211 and 20773122), External Cooperation Program of Chinese Academy of Sciences (GJHZ200827).

Appendix A. Supplementary data

Supplementary data associated with this article can be found, in the online version, at http://dx.doi.org/10.1016/j.apcatb.2012.10.001.

References

[1] V. Zakirov, V. Goeman, T.J. Lawrence, M.N. Sweeting, Proceedings of the 14th Annual AIAA/USU Conference on Small Satellites, USA, 21–24 August, 2000.
[2] J.R. Wallbank, P.A. Sermon, A.M. Barker, L. Courtney, R.M. Sambrook, Space Propulsion 2004, Italy, 7–8 June, 2004.
[3] V. Zakirov, H. Zhang, Aerosol Science and Technology 12 (2008) 318–323.
[4] E.V. Kondratenko, V. Gölden, S. Sokolov, ChemCatChem 2 (2010) 633–635.
[5] V. Gölden, S. Sokolov, V.A. Kondratenko, E.V. Kondratenko, Applied Catalysis B 101 (2010) 130–136.
[6] S. Kannan, C.S. Swamy, Catalysis Today 53 (1999) 725–737.
[7] J.N. Armor, T.A. Braymer, T.S. Farris, Y. Li, F.P. Petrocelli, E.L. Weist, S. Kannan, C.S. Swamy, Applied Catalysis B 7 (1996) 397–406.
[8] J.A.Z. Pieterse, S. Booneveld, R.W. van den Brink, Applied Catalysis B 51 (2004) 215–228.
[9] J. Pérez-Ramírez, F. Kapteijn, G. Mul, J.A. Moulijn, Chemical Communications 8 (2001) 693–694.
[10] R.S. da Cruz, A.J.S. Mascarenhas, H.M.C. Andrade, Applied Catalysis B 18 (1998) 223–231.
[11] Y. Li, J.N. Armor, Applied Catalysis B 1 (1992) L21–L29.

[12] H. Zeng, X. Pang, Applied Catalysis B 13 (1997) 113–122.
[13] S. Kawi, S. Liu, S.-C. Shen, Catalysis Today 68 (2001) 237–244.
[14] F. Kapteijn, J. Rodriguez-Mirasol, J.A. Moulijn, Applied Catalysis B 9 (1996) 25–64.
[15] H. Rodhe, Science 248 (1990) 1217–1219.
[16] J.G. McCarty, M.I. Gusman, D.M. Lowe, D.L. Hildenbrand, K.N. Lau, Catalysis Today 47 (1999) 5–17.
[17] D.J. Haynes, A. Campos, D.A. Berry, D. Shekhawat, A. Roy, J.J. Spivey, Catalysis Today 155 (2010) 84–91.
[18] H. Huang, W. Li, H. Liu, Catalysis Today 183 (2012) 58–64.
[19] N. Russo, D. Fino, G. Saracco, Catalysis Today 119 (2007) 228–232.
[20] D.M. Lowe, M.I. Gusman, J.G. McCarty, Studies in Surface Science and Catalysis 91 (1995) 445–452.
[21] M. Machida, K. Eguchi, H. Arai, Journal of Catalysis 123 (1990) 477–485.
[22] T. Utaka, S.A. Al-Drees, J. Ueda, Y. Iwasa, T. Takeguchi, R. Kikuchi, K. Eguchi, Applied Catalysis A 247 (2003) 125–131.
[23] H. Arai, M. Machida, Applied Catalysis A 138 (1996) 161–176.
[24] K. Eguchi, H. Arai, Catalysis Today 29 (1996) 379–386.
[25] N. Iyi, S. Takekawa, S. Kimura, Journal of Solid State Chemistry 83 (1989) 8–19.
[26] G. Groppi, M. Bellotto, C. Cristiani, P. Forzatti, Journal of Materials Science 34 (1999) 2609–2620.
[27] G. Groppi, C. Cristiani, P. Forzatti, Applied Catalysis B 35 (2001) 137–148.
[28] M. Tian, A. Wang, X. Wang, Y. Zhu, T. Zhang, Applied Catalysis B 92 (2009) 437–444.
[29] Y. Zhu, X. Wang, A. Wang, G. Wu, J. Wang, T. Zhang, Journal of Catalysis 283 (2011) 149–160.
[30] S. Zhu, X. Wang, A. Wang, Y. Cong, T. Zhang, Chemical Communications (2007) 1695–1697.
[31] S. Zhu, X. Wang, A. Wang, T. Zhang, Catalysis Today 131 (2008) 339–346.
[32] R. Kikuchi, Y. Iwasa, T. Takeguchi, K. Eguchi, Applied Catalysis A 281 (2005) 61–67.
[33] J. Wang, X. Bokhimi, A. Morales, O. Novaro, T. López, R. Gómez, Journal of Physical Chemistry B 103 (1999) 299–303.
[34] G. Groppi, M. Bellotto, C. Cristiani, P. Forzatti, P.L. Villa, Applied Catalysis A 104 (1993) 101–108.
[35] G. Groppi, C. Cristiani, P. Forzatti, M. Bellotto, Journal of Materials Science 29 (1994) 3441–3450.
[36] P.C. Donohue, L. Kata, R. Ward, Inorganic Chemistry 4 (1965) 306–310.
[37] J.A. Kafalas, J.M. Longo, Materials Research Bulletin 3 (1968) 687–692.
[38] Y. Cai, Z. Huang, X. Meng, X. Ming, C. Wang, G. Chen, Solid State Sciences 13 (2011) 350–355.
[39] D. Verdoes, H.W. Zandbergen, D.J.W. Ijdo, Materials Research Bulletin 22 (1987) 1–10.
[40] M.S. Yalfani, M. Santiago, J. Pérez-Ramírez, Journal of Materials Chemistry 17 (2007) 1222–1229.
[41] N. Iyi, Z. Inoue, S. Takekawa, S. Kimura, Journal of Solid State Chemistry 52 (1984) 66–72.
[42] M. Bellotto, G. Artioli, C. Cristiani, P. Forzatti, G. Groppi, Journal of Catalysis 179 (1998) 597–605.
[43] E. Tronc, F. Laville, M. Gasperin, A.M. Lejus, D. Vivien, Journal of Solid State Chemistry 81 (1989) 192–202.
[44] A. Modaressi, A. Courtois, R. Gerardin, B. Malaman, C. Gleitzer, Journal of Solid State Chemistry 47 (1983) 245–255.
[45] F. Kapteijn, G. Marbán, J. Rodriguez-Mirasol, J.A. Moulijn, Journal of Catalysis 167 (1997) 256–265.
[46] C.M. Fu, V.N. Korchar, W.K. Hall, Journal of Catalysis 68 (1981) 166–171.
[47] J.A. Ryder, A.K. Chakraborty, A.T. Bell, Journal of Catalysis 220 (2003) 84–91.
[48] G. Groppi, F. Assandri, M. Bellotto, C. Cristiani, P. Forzatti, Journal of Solid State Chemistry 114 (1995) 326–336.